Nano Research

Open Access

Research Article

Efficient single-atom Ru catalysts constructed by ligand engineering-thermal reduction synergy strategy for alkene hydrosilylation

Yu Luo[1], Xinping Yan[1], Sen Wang[1], Yanzhao Dong[1] ✉, Bao Wang[1], Jinli Zhang[1,2], and Haiyang Zhang[1] ✉

[1] *School of Chemistry and Chemical Engineering, Shihezi University, Shihezi 832000, China*
[2] *School of Chemical Engineering and Technology, Tianjin University, Tianjin 300072, China*

Cite this article: *Nano Research*, **2026**, *19*, 94908513. https://doi.org/10.26599/NR.2026.94908513

ABSTRACT: The excellent activity of platinum-based catalysts in the hydrosilylation of alkenes is limited by their high cost, which has led to the emergence of ruthenium as a cost-effective alternative with promising prospects; however, the relatively low catalytic activity of Ru catalysts remains a major challenge. Herein, a ligand engineering-thermal reduction synergistic (LETRS) strategy was employed to construct single-atom Ru catalysts (Ru-MLDZ$_{2:1}$/AC-H$_2$, where MLDZ denotes N-methylimidazole and AC denotes activated carbon), which demonstrated excellent activity and selectivity for the hydrosilylation of alkenes. Under solvent-free conditions at 60 °C, Ru-MLDZ$_{2:1}$/AC-H$_2$ exhibited comparable catalytic efficiency to platinum-based catalysts, with its alkene conversion rate being approximately 37% higher than that of Ru/AC. Experimental results combined with density functional theory (DFT) calculations demonstrate that the unique coordination environment of Ru-MLDZ$_{2:1}$/AC-H$_2$ exhibits strong affinity toward triethoxysilane, which facilitates efficient Si–H bond activation and reduces the energy barrier in the rate-determining step, consequently leading to significantly enhanced catalytic activity. This study provides a new strategy and valuable insights for designing highly active and economically viable heterogeneous single-atom catalysts.

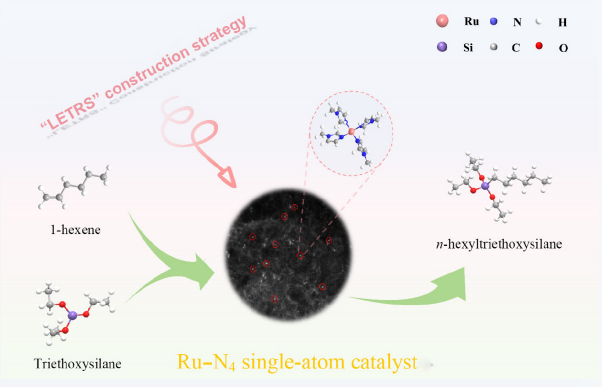

KEYWORDS: hydrosilylation of alkenes, single-atom Ru, heterogeneous catalysts, ligand engineering-thermal reduction synergistic, Si–H bond activation

1 Introduction

Organosilicon compounds are widely used in various fields, such as organic synthesis, pharmaceutical engineering, aerospace, and national defense, due to their unique chemical and physical properties [1–5]. The hydrosilylation of alkenes is one of the most important and widely used reactions for the synthesis of alkylsilanes in organosilicon chemistry. In this process, the Si–H bonds are efficiently added to the C=C bond of alkenes to form new C–Si bonds [6, 7]. With its excellent atomic economy, high selectivity, and mild reaction conditions, the hydrosilylation of alkenes has become a key reaction in the organosilicon industry [8–10]. Currently, the hydrosilylation reactions mainly rely on homogeneous Pt catalysts (such as Karstedt catalyst and Speier catalyst) in the industrial field [11, 12]. However, these homogeneous catalytic systems have limitations, such as low selectivity of the target product, waste of precious metal resources, and difficulty in catalyst recovery. Therefore, the development of heterogeneous catalysts with excellent catalytic performance and recyclability has become an important direction for the future development of the hydrosilylation of alkenes.

In recent years, researchers have attempted to prepare heterogeneous catalysts using precious metals (such as Pt, Rh, and Ir) to improve catalytic activity and selectivity of alkyl silane, while achieving the recovery and reuse of the catalysts [13–18]. However, due to the high cost of these precious metals, their economic benefits in practical industrial applications are rather limited. In contrast, ruthenium (Ru), as a relatively inexpensive precious metal, has a significantly lower cost than rhodium (Rh), platinum (Pt), and iridium (Ir), making it an ideal candidate for the development of hydrosilylation catalysts. For example, Masato et al. synthesized a homogeneous Ru-based catalyst using $Ru_3(CO)_{12}$ as the active component to catalyze the hydrosilylation of allyl chloride and

Received: December 29, 2025; **Revised:** January 26, 2026
Accepted: January 30, 2026

✉Address correspondence to Yanzhao Dong, dongyanzhao2012@163.com; Haiyang Zhang, zhy198722@163.com

trimethoxysilane. Eventually, 3-chloropropyl-trimethoxysilane with a yield of 70% was obtained [19]. Kanbur et al. prepared a heterogeneous $Cp^*RuH(SiH_2Ph)_2(PCy_3)/SO_4/ZrO_2$ (PCy_3 denotes tricyclohexylphosphine) catalyst by surface organometallic chemistry techniques using $Cp^*RuH(SiH_2Ph)_2(PCy_3)$ as the active precursor and sulfated zirconia as the support to catalyze the hydrosilylation of cyclohexene and phenylsilane ($PhSiH_3$), achieving a yield of 88% for cyclohexylphenylsilane [20]. Although Ru-based catalysts have demonstrated promising potential in alkene hydrosilylation reactions, several critical challenges remain to be urgently addressed. First, the unsatisfactory regioselectivity and chemoselectivity of the catalytic reactions result in diminished yields of the desired products. Second, the active centers are prone to undergoing structural transformation or deactivation under reaction conditions. Additionally, insufficient dispersion of the active species on the support limits the effective utilization of active sites. These factors collectively constrain the catalytic efficiency of Ru-based catalysts and hinder their implementation in industrial-scale applications [5, 21].

Single-atom catalysts (SACs) have the characteristics of high atomic utilization and well-defined active center structures, bridging the gap between homogeneous and heterogeneous systems [22–26]. Some heterogeneous single-atom catalysts have already demonstrated catalytic performance comparable to, or even better than, that of homogeneous catalysts. Therefore, the development of heterogeneous Ru SACs with high atomic utilization and excellent catalytic performance and their application in the hydrosilylation of alkenes are highly desirable. Recently, many SACs have been reported for the hydrosilylation of alkenes. For example, Han et al. prepared a $PtFe_3$/CN (CN denotes carbon nitride) catalyst with ordered and single-dispersed Pt sites using an *in-situ* location-restricted migration (LRM) strategy. In the hydrosilylation of 1-octene with triethoxysilane (TES), $PtFe_3$/CN catalyst showed excellent catalytic activity (1-octene conversion of ~ 99%), which was much higher than that of Pt nanoparticles (NPs)/CN catalyst (~ 55%) and commercial Pt/C catalyst (~ 25%) [27]. Yang et al. constructed Pt_1-N-C catalysts with atomically dispersed Pt species supported on carbon black by the interfacial spontaneous reduction (ISR) method to catalyze the hydrosilylation of 1-octene and triethoxysilane. The catalytic activity of Pt_1-N-C reached as high as 4.5×10^5 h^{-1}, far exceeding that of the traditional Speier catalyst (1.8×10^5 h^{-1}), Pt NP-N-P (2.8×10^5 h^{-1}), and commercial Pt/C catalyst (1.7×10^5 h^{-1}) [28]. Li et al. developed a heterogeneous catalyst with atomically dispersed Ru species under a reductive atmosphere, which exhibited excellent catalytic activity in the hydrosilylation of ethylene with triethoxysilane [29]. However, the specific existence state of active species in these catalysts has not yet been clearly identified, and there is a lack of guidance for the design of efficient catalysts. In addition, the preparation of these single-atom catalysts generally involves complex synthetic steps, expensive chemicals, and harsh high-temperature calcination treatments, which limit their feasibility for industrial application.

This work presents a preparation strategy that combines ligand coordination chemistry and thermal reduction, successfully synthesizing a single-atom Ru catalyst (Ru-$MLDZ_{2:1}$/AC-H_2, where MLDZ denotes N-methylimidazole and AC denotes activated carbon) loaded on activated carbon. Then, the hydrosilylation of 1-hexene with TES was used as a model reaction to investigate the catalytic performance of Ru-$MLDZ_{2:1}$/AC-H_2. The experimental results demonstrate that this catalyst exhibits extremely high catalytic activity and selectivity. Density functional theory (DFT) calculations demonstrate that the energy barrier for hydrosilylation of 1-hexene over Ru-$MLDZ_{2:1}$/AC-H_2 is significantly lower than that of Ru/AC, leading to enhanced catalytic performance. This enhancement can be ascribed to the unique electronic and geometrical features of the monodisperse Ru species, which facilitate the efficient release of products.

2 Experimental section

2.1 Materials

Coconut-based AC was purchased from Fujian Sensen Carbon Industry Technology Co., Ltd. Ruthenium(III) chloride trihydrate (Ru: 37%, premium grade), MLDZ (> 99%), imidazole (IMDZ, > 99%), 2-methylimidazole (DMDZ, > 99%), N-propylimidazole (PMDZ, > 99%), N-isopropylimidazole (IPMDZ, > 99%), N-allylimidazole (AMDZ, > 99%), 1-hexene (> 99%), TES (> 99%), and *n*-heptane (C_7H_{16}, > 99%) were obtained from Adamas. Ethanol (≥ 99.7%), hydrochloric acid (36%–38%), and other reagents were provided by Tianjin Fuyu Fine Chemical Co., Ltd.

2.2 Synthesis of catalysts

2.2.1 *Synthesis of Ru-imidazole-based ligands (IMIs)/AC catalysts*

In a 100 mL beaker, 0.012 g of MLDZ was dissolved in 20 mL of anhydrous ethanol to prepare Solution A. Subsequently, 7.56 mL of $RuCl_3{\cdot}3H_2O$ ethanol solution (0.01 g/mL) was added to Solution A. After ultrasonication, the precursor Solution B was obtained. Under stirring, 2.86 g of activated carbon was added to the precursor Solution B, and the mixture was impregnated for 12 h. After impregnation, the sample was dried in a 70 °C water bath for 7 h. The dried sample was then washed sequentially with ultrapure water and anhydrous ethanol to remove unbound Ru species. Finally, the solid product was dried in a 60 °C vacuum oven for 12 h, obtaining the Ru-$MLDZ_{1:1}$/AC catalyst (where the molar ratio of Ru to MLDZ was 1:1). Following the same procedures, other Ru-based catalysts coordinated with different imidazole-based ligands were also prepared, including Ru-$IMDZ_{1:1}$/AC, Ru-$DMDZ_{1:1}$/AC, Ru-$PMDZ_{1:1}$/AC, Ru-$IPMDZ_{1:1}$/AC, and Ru-$AMDZ_{1:1}$/AC (where IMDZ, DMDZ, PMDZ, IPMDZ, and AMDZ represent imidazole, 2-methylimidazole, N-propylimidazole, N-isopropylimidazole, and N-allylimidazole, respectively). Additionally, Ru catalysts with different molar ratios of Ru to MLDZ were prepared following the same method, including Ru-$MLDZ_{1:2}$/AC, Ru-$MLDZ_{1:1}$/AC, Ru-$MLDZ_{2:1}$/AC, Ru-$MLDZ_{3:1}$/AC, and Ru-$MLDZ_{4:1}$/AC. For comparison, Ru/AC was also prepared by an analogous procedure in the absence of the imidazole ligand. Among these, the Ru loadings of Ru-$MLDZ_{2:1}$/AC and Ru/AC were determined to be 0.65 wt.% and 0.74 wt.% by inductively coupled plasma-optical emission spectroscopy (ICP-OES) analysis (Table S1 in the Electronic Supplementary Material (ESM)).

2.2.2 *Synthesis of Ru/AC-H_2 and Ru-$MLDZ_{2:1}$/AC-H_2 catalysts*

The Ru-$MLDZ_{2:1}$/AC-H_2 and Ru/AC-H_2 samples were obtained by reducing the Ru-$MLDZ_{2:1}$/AC and Ru/AC catalysts at 160 °C under an atmosphere of H_2/Ar mixture (30% H_2) for 1 h, and the Ru loadings of Ru/AC-H_2 and Ru-$MLDZ_{2:1}$/AC-H_2 were determined by ICP-OES to be 0.73 wt.% and 0.63 wt.%, respectively (Table S1 in the ESM).

3 Results and discussion

3.1 Catalytic performance evaluation of Ru-based catalysts

In the hydrosilylation reaction of 1-hexene with TES (Fig. 1(a)), the evaluation results of catalytic performance revealed that the Ru-IMIs/AC complex catalysts prepared with imidazole-based ligands exhibited higher catalytic activity and selectivity compared to the Ru/AC catalyst (Fig. 1(b) and Fig. S1 in the ESM). Among these catalysts, the Ru-MLDZ/AC catalyst prepared using MLDZ as the ligand exhibited the best catalytic performance, achieving a 1-hexene conversion of 61.84%, which represented an increase of 14.85% compared to the Ru/AC catalyst, with the selectivity to β-adduct reaching 98.93%. This improved catalytic performance can be attributed to the coordination interaction between N-methylimidazole and ruthenium.

To further improve the catalytic performance of Ru-MLDZ/AC, the molar ratio between Ru and MLDZ ligand was optimized (Fig. 1(c) and Fig. S2 in the ESM). When the Ru/MLDZ molar ratio was 1:2, the catalytic performance of the Ru-$MLDZ_{1:2}$/AC catalyst decreased significantly compared to the Ru/AC catalyst, with the 1-hexene conversion dropping below 10% and the selectivity to the β-addition product also being relatively low. This could be due to the precipitation of Ru species during complexation with excess ligand, resulting in incomplete loading of Ru onto the activated carbon support. As the amount of MLDZ ligand decreased, the conversion of 1-hexene first increased and then declined; nonetheless, all Ru-MLDZ catalysts with molar ratios of 1:1, 2:1, 3:1, and 4:1 outperformed the Ru/AC catalyst. The optimal catalytic performance was achieved over Ru-$MLDZ_{2:1}$/AC with a Ru/MLDZ molar ratio of 2:1, reaching a 1-hexene conversion of 68.48%. Further reduction of the MLDZ dosage led to a decline in conversion, but the performance was still superior to that of the Ru/AC catalyst. These results indicate that an appropriate molar ratio of Ru/MLDZ can effectively modulate the coordination environment of Ru species and thus enhance catalytic performance. Therefore, the optimal molar ratio of Ru/MLDZ is determined to be 2:1.

Subsequently, the Ru/AC and Ru-$MLDZ_{2:1}$/AC catalysts were subjected to thermal reduction under a reductive atmosphere for 1 h (denoted as Ru/AC-H_2 and Ru-$MLDZ_{2:1}$/AC-H_2), and their catalytic performances for the hydrosilylation of 1-hexene with TES were also evaluated (Fig. 1(d) and Fig. S3 in the ESM). The experimental results showed that the reduction treatment prolonged the induction period of the catalytic reaction. Nevertheless, the catalytic activities of these two reduced catalysts (Ru/AC-H_2 and Ru-$MLDZ_{2:1}$/AC-H_2) were improved to varying

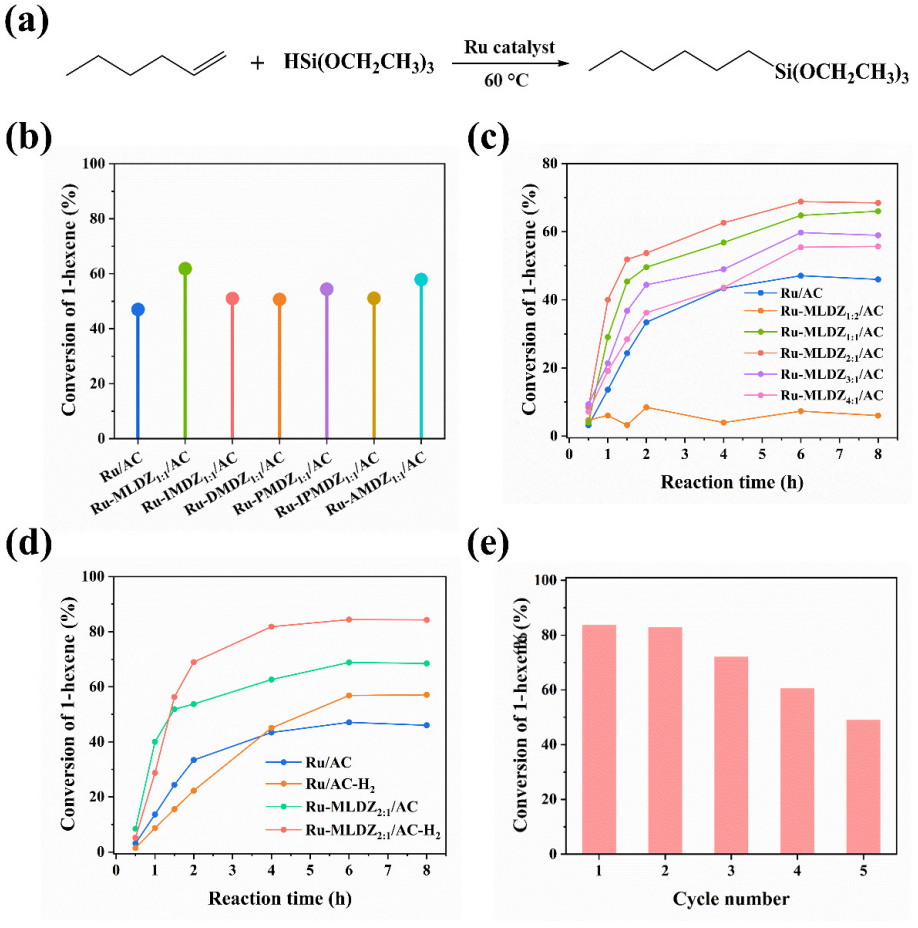

Figure 1 (a) Scheme of Ru-catalyzed hydrosilylation between 1-hexene and triethoxysilane at 60 °C under solvent-free conditions. (b) Conversion of 1-hexene over different Ru-based catalysts at the reaction time of 6 h. (c) Effect of the molar ratio of ruthenium and MLDZ ligand on hydrosilylation of 1-hexene over Ru-MLDZ/AC catalysts. (d) Plots of conversion versus time for Ru/AC, Ru/AC-H_2, Ru-$MLDZ_{2:1}$/AC, and Ru-$MLDZ_{2:1}$/AC-H_2. (e) Recyclability test on Ru-$MLDZ_{2:1}$/AC-H_2. Reaction conditions: T = 60 °C, N = 500 r/min, $n_{1\text{-hexene}}/n_{TES}$ = 1, and n_{Ru}/n_{TES} = 1:1500 (T, N, $n_{1\text{-hexene}}$, n_{TES}, and n_{Ru} denote the reaction temperature, rotation speed, molar amount of 1-hexene, molar amount of triethoxysilane, and molar amount of ruthenium, respectively).

degrees compared to the two reference catalysts. For Ru/AC-H_2, the conversion of 1-hexene reached 56.84% after 6 h, which was 8.85% higher than that of the untreated Ru/AC. Similarly, for Ru-MLDZ$_{2:1}$/AC-H_2, the conversion of 1-hexene reached 84.41%, which was higher than that of Ru-MLDZ$_{2:1}$/AC (68.48%). These findings further demonstrate that the thermal reduction process is effective in boosting the catalytic performance of Ru-based catalysts. This is likely due to the formation of a greater proportion of low-valent Ru species during the reduction treatment. In addition, the reusability of Ru-MLDZ$_{2:1}$/AC-H_2 is shown in Fig. 1(e). The conversion of 1-hexene remained stable during the first two cycles, after which it exhibited a consistent decline. By the fifth cycle, the conversion decreased significantly from the initial 83.64% to 48.99%. To elucidate the reasons for the catalyst deactivation, systematic characterization analyses were conducted on both fresh and recycled catalyst samples. First, X-ray photoelectron spectroscopy (XPS) was employed to investigate the evolution of the chemical valence states of Ru species. XPS analysis shows no significant shift in the Ru binding energy or change in the average Ru oxidation state between the fresh and recycled catalysts, indicating that the chemical valence of Ru remains stable throughout the cycling process (Fig. S4 and Table S2 in the ESM). Meanwhile, X-ray diffraction (XRD) patterns (Fig. S5 in the ESM) demonstrate that no characteristic diffraction peaks attributable to Ru nanoparticles are observed in the recycled catalyst, suggesting that Ru species maintain a highly dispersed state after the reaction. However, the quantitative analysis by ICP-OES reveals that the actual Ru loading in Ru-MLDZ$_{2:1}$/AC-H_2 decreases from the initial 0.63 wt.% to 0.28 wt.% after five cycles (Fig. S6 in the ESM), confirming significant leaching of Ru species during the recycling process. Comprehensive analysis indicates that the decline in the recycling performance of the Ru-MLDZ$_{2:1}$/AC-H_2 catalyst is primarily attributed to the leaching loss of active Ru species during the cycling process. This phenomenon represents a critical issue that urgently requires resolution and will be the focus of improvement in our future work.

In order to deeply explore the internal structural characteristics of the catalysts and the internal factors that affect the catalytic performance, a series of characterization techniques was carried out.

3.2 Characterizations of Ru-based catalysts

To investigate the distribution of Ru species on various ruthenium catalysts, aberration-corrected high-angle annular dark-field scanning transmission electron microscopy (AC-HAADF-STEM) characterization techniques were employed. As observed from AC-HAADF-STEM images, the Ru/AC catalyst contains relatively large Ru nanoparticles with an average particle diameter of 1.80 ± 0.02 nm (Fig. 2(a) and Fig. S7 in the ESM). In contrast, the Ru species on Ru/AC-H_2 sample exhibits smaller particle sizes (Fig. 2(b)), indicating that the reduction treatment could enhance the dispersion of Ru species. Compared to Ru/AC, the Ru-MLDZ$_{2:1}$/AC catalyst prepared via coordination with the MLDZ ligand shows significantly smaller Ru species, which are uniformly dispersed on the activated carbon in the form of both Ru clusters and isolated Ru single atoms (Fig. 2(c)). After thermal reduction, the Ru species on Ru-MLDZ$_{2:1}$/AC-H_2 are observed to be atomically dispersed on the support surface (Fig. 2(d)), suggesting that the low-temperature reduction process further promotes the dispersion of Ru species. This enhancement may be attributed to the ability of hydrogen to facilitate metal dispersion during mild thermal treatment [30, 31]. Elemental mapping of the Ru-MLDZ$_{2:1}$/AC-H_2 sample reveals a homogeneous distribution of C, N, Ru, and Cl elements (Fig. 2(e)), further confirming the high dispersion of Ru species on the activated carbon support [32].

XRD patterns of all Ru-based catalysts display only two broad diffraction peaks at 22.5° and 43.5°, corresponding to amorphous carbon (Fig. 2(f)) [33]. No characteristic diffraction peaks attributable to metallic Ru are observed in the XRD patterns, indicating that Ru species exist in a highly dispersed state on the catalyst or that the crystallite size is below the detection limit of XRD. Based on the above characterizations, the introduction of imidazole ligands and thermal reduction treatment significantly improves the dispersion of Ru species, which also ensures that the active species maintain high activity and stability during the reaction.

To further investigate the pore structure characteristics of the catalysts, nitrogen (N_2) adsorption–desorption measurements were performed. As shown in Fig. 2(g), all catalysts, including Ru/AC, Ru/AC-H_2, Ru-MLDZ$_{2:1}$/AC, and Ru-MLDZ$_{2:1}$/AC-H_2, exhibit typical Type-IV isotherms with H4-type hysteresis loops. All these catalysts exhibit high N_2 adsorption capacity in the range of low relative pressure ($P/P_0 < 0.1$), indicating significant microporous and mesoporous structures exist in these catalysts [34, 35]. As listed in Table S3 in the ESM, the specific surface areas (1625, 1630, 1637, and 1634 m^2/g), average pore sizes (1.99, 2.04, 2.02, and 2.04 nm), and pore volumes (0.66, 0.64, 0.66, and 0.65 cm^3/g) of all these catalysts are similar. These results suggest that the introduction of ligands and the subsequent thermal reduction treatment exert negligible effects on the textural parameters of the catalysts.

To clarify the effect of imidazole-based ligand coordination and thermal reduction treatment on the valence states of Ru active species and their interaction with the support, H_2-temperature-programmed reduction (TPR) characterization was conducted for all Ru-based catalysts (Fig. 2(h)). From the H_2-TPR profiles, it can be observed that a reduction peak appears in the range of 400–800 °C, which is attributed to the reduction of oxygen-containing functional groups on the support surface. Apart from that, two characteristic reduction peaks of Ru species are also observed in the range of 100–300 °C. Specifically, for the Ru/AC catalyst, the peaks at 206 and 250 °C correspond to the reduction of RuO_2 and Ru^{3+} species, respectively. Compared to the benchmark Ru/AC catalyst, the reduction peaks of RuO_2 and Ru^{3+} in Ru-MLDZ$_{2:1}$/AC shift to higher temperatures, indicating a strong interaction between Ru species and imidazole ligands. In addition, the Ru-MLDZ$_{2:1}$/AC catalyst exhibits increased peak areas of both RuO_2 and Ru^{3+} species, indicating that coordination with the MLDZ ligand significantly enhances the formation of these oxidized Ru species. Furthermore, comparing the TPR profiles of Ru/AC and Ru-MLDZ$_{2:1}$/AC before and after thermal reduction, it is found that the intensity of peaks corresponding to high-valence Ru species decreases significantly after reduction treatment, suggesting that the thermal treatment effectively promotes their transformation into lower-valent Ru species. Notably, the reduction temperatures of RuO_2 and Ru^{3+} species also decrease significantly after reduction treatment. This shift is attributed to the increased content of metallic Ru species, which facilitates hydrogen spillover. The reducing ability of the escaped hydrogen atoms is higher than that of molecular hydrogen, which lowers the energy barrier of reduction and thus reduces the reduction temperature required [36–38]. These results collectively indicate that the incorporation of

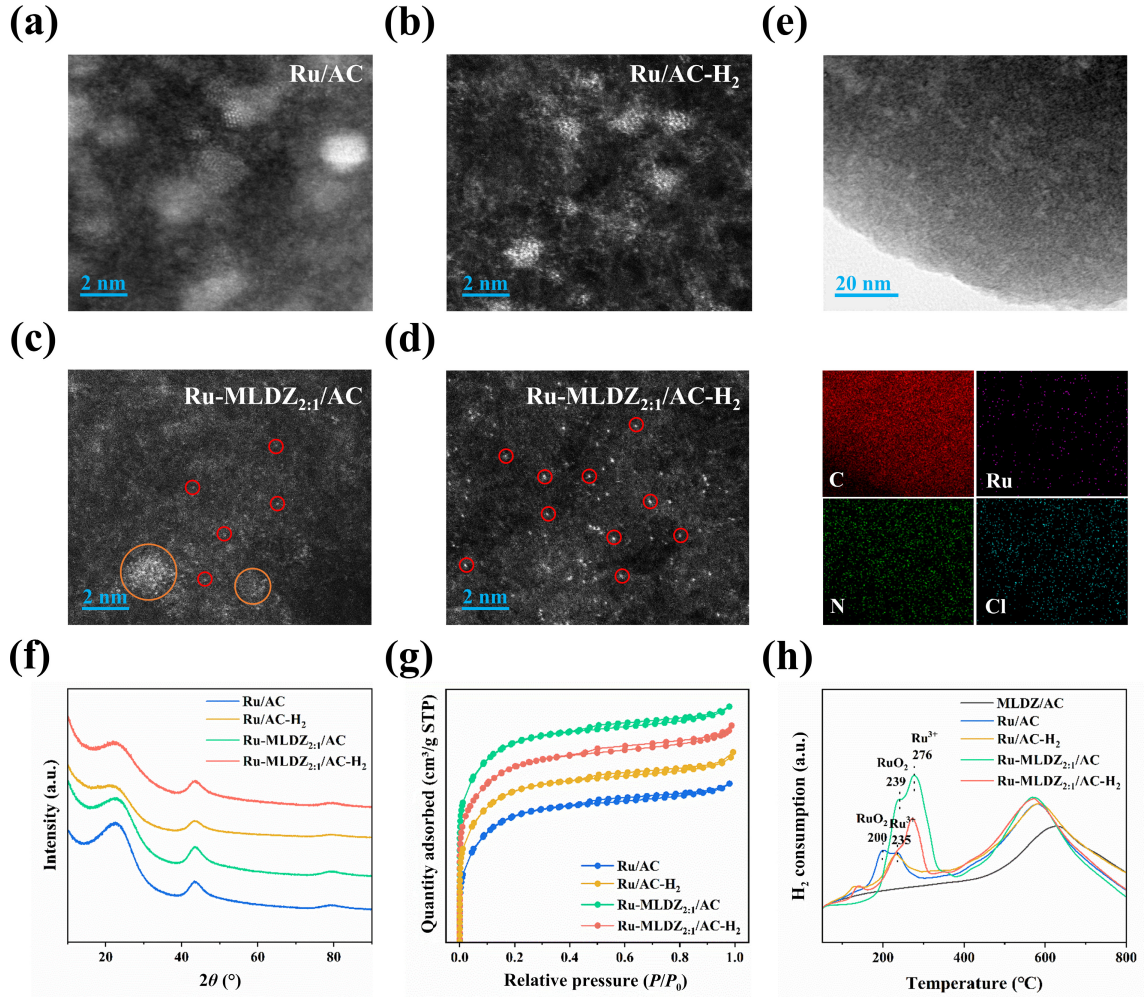

Figure 2 AC-HAADF-STEM images of the (a) Ru/AC, (b) Ru/AC-H_2, (c) Ru-MLDZ$_{2:1}$/AC, and (d) Ru-MLDZ$_{2:1}$/AC-H_2 (the red circles highlight single atoms, whereas the yellow ones indicate clusters). (e) Energy-dispersive X-ray spectroscopy (EDS) mapping of C, N, Ru, and Cl in Ru-MLDZ$_{2:1}$/AC-H_2. (f) XRD patterns of Ru/AC, Ru/AC-H_2, Ru-MLDZ$_{2:1}$/AC, and Ru-MLDZ$_{2:1}$/AC-H_2. (g) N_2 adsorption–desorption isotherms for Ru/AC, Ru/AC-H_2, Ru-MLDZ$_{2:1}$/AC, and Ru-MLDZ$_{2:1}$/AC-H_2. (h) H_2-TPR curves of the Ru catalysts.

imidazole ligands and the thermal reduction treatment distinctly modulate the electronic structure of Ru species within the catalyst.

To further investigate the electronic structure of the active species in catalyst, the surface properties of the catalyst were analyzed by XPS spectra [39, 40]. It can be seen from Figs. 3(a) and 3(b) and Table S4 in the ESM that the peak position of Ru species in Ru-MLDZ$_{2:1}$/AC shifts to higher binding energies compared to those in Ru/AC, indicating that the introduced imidazole ligand interacts with the Ru precursor and reduces the electron density of Ru species. Furthermore, compared to Ru/AC, the Ru-MLDZ$_{2:1}$/AC catalyst shows increased relative contents of Ru^{3+} species, while the content of RuO_2 decreases. This observation suggests that the coordination between Ru atoms and nitrogen atoms of the imidazole ring facilitates electron transfer from Ru species to the ligand, resulting in an increase of Ru^{3+} species.

After thermal reduction of both Ru/AC and Ru-MLDZ$_{2:1}$/AC catalysts (Ru/AC-H_2 and Ru-MLDZ$_{2:1}$/AC-H_2), a significant increase in the proportions of Ru^{3+} and Ru^0 species is observed, accompanied by a corresponding decrease in RuO_2 content. These findings demonstrate that thermal reduction treatment effectively facilitates the reduction of high-valence Ru species (RuO_2) into lower-valence forms (Ru^{3+} and Ru^0), which is consistent with the H_2-TPR results. Combined with catalytic performance evaluations, it can be concluded that low-valent Ru species (Ru^0 and Ru^{3+}) are the primary active sites for the hydrosilylation of 1-hexene with TES. In addition, for the N species, the binding energy positions of pyridinic N (397.9 eV) and pyrrolic N (399.8 eV) in Ru-MLDZ$_{2:1}$/AC shift to lower binding energies compared to those of pyridinic N (398.0 eV) and pyrrolic N (400.1 eV) in Ru/AC (Fig. 3(c)). Additionally, the content of pyrrolic N decreases, while the proportion of graphitic N increases significantly (Table S5 in the ESM). These changes further prove the presence of strong electronic interactions between the Ru precursor and the imidazole ligand. Overall, these results demonstrate that the introduction of imidazole ligands significantly modulates the electronic structure of Ru species, while thermal reduction further improves the proportion of active Ru^{3+} and Ru^0 species, thereby improving the catalytic performance of heterogeneous Ru-based catalysts for hydrosilylation of alkenes. Subsequently, in order to further investigate the electronic structure and coordination environment of Ru species, X-ray absorption spectroscopy (XAS) was used to characterize the catalyst [41, 42]. As shown in Fig. 3(d), the Ru K-edge X-ray absorption near-edge structure (XANES) spectra reveal that the white line peak position of Ru/AC is located between those

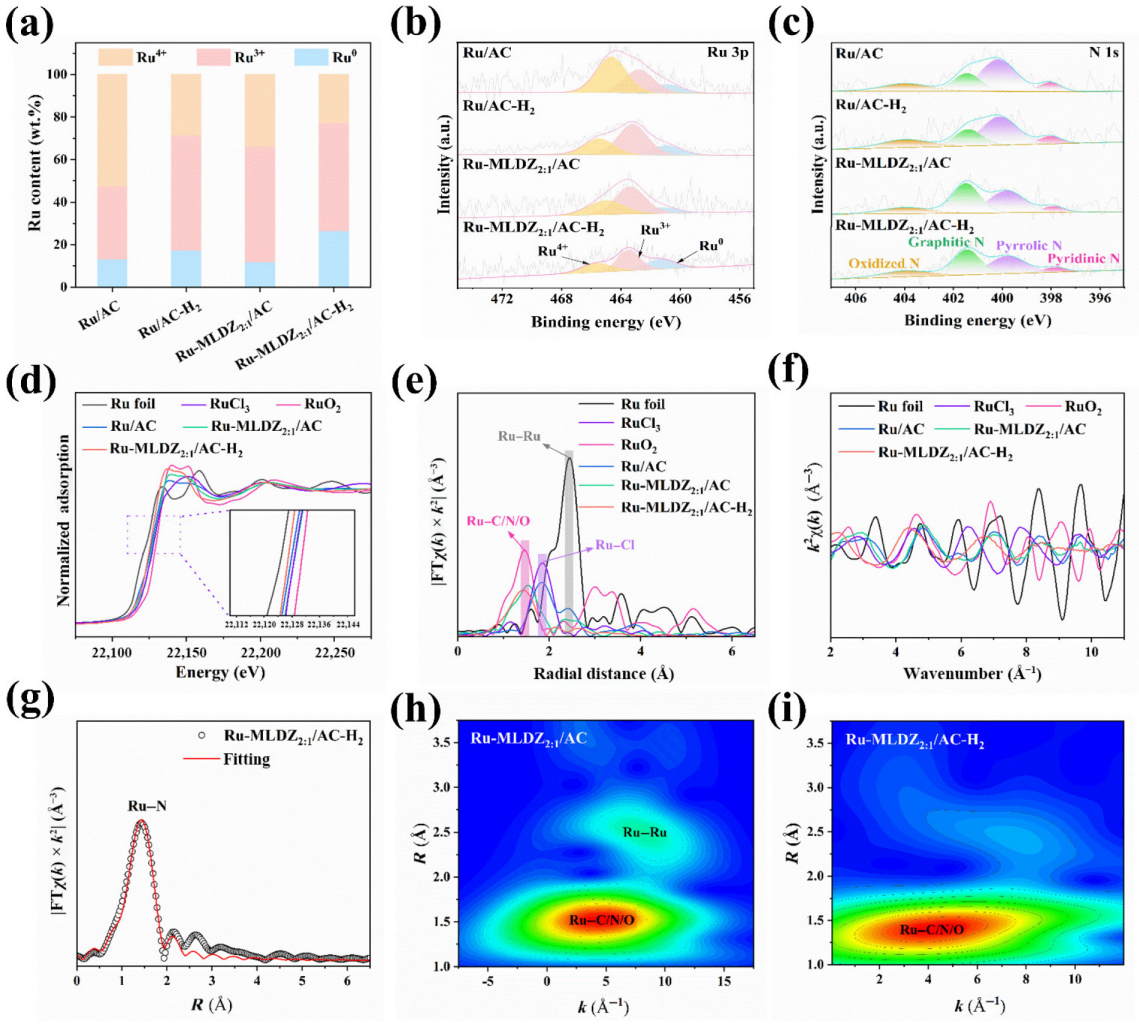

Figure 3 (a) The contents of various Ru species in Ru/AC, Ru/AC-H_2, Ru-$MLDZ_{2:1}$/AC, and Ru-$MLDZ_{2:1}$/AC-H_2 catalysts. (b) Ru 3p spectra of Ru/AC, Ru/AC-H_2, Ru-$MLDZ_{2:1}$/AC, and Ru-$MLDZ_{2:1}$/AC-H_2 catalysts. (c) N 1s spectra of Ru/AC, Ru/AC-H_2, Ru-$MLDZ_{2:1}$/AC, and Ru-$MLDZ_{2:1}$/AC-H_2 catalysts. (d) XANES spectra of Ru K-edges for Ru foil, $RuCl_3$, RuO_2, Ru/AC, Ru-$MLDZ_{2:1}$/AC, Ru-$MLDZ_{2:1}$/AC-H_2, and derived Ru K-edge XANES spectra of Ru foil, $RuCl_3$, RuO_2, Ru/AC, Ru-$MLDZ_{2:1}$/AC, and Ru-$MLDZ_{2:1}$/AC-H_2. (e) Fourier transform (FT) EXAFS spectra of Ru foil, $RuCl_3$, RuO_2, Ru/AC, Ru-$MLDZ_{2:1}$/AC, and Ru-$MLDZ_{2:1}$/AC-H_2. (f) $k^2\chi(k)$ EXAFS analysis of Ru foil, $RuCl_3$, RuO_2, Ru/AC, Ru-$MLDZ_{2:1}$/AC, and Ru-$MLDZ_{2:1}$/AC-H_2 catalysts. (g) FT-EXAFS spectra of Ru-$MLDZ_{2:1}$/AC-H_2. Wavelet transform of k^2-weighted EXAFS signals of (h) Ru-$MLDZ_{2:1}$/AC and (i) Ru-$MLDZ_{2:1}$/AC-H_2.

of Ru foil and $RuCl_3$, indicating that the oxidation state of Ru in Ru/AC falls between 0 and +3. After ligand coordination, the white line peak position of the Ru-$MLDZ_{2:1}$/AC catalyst also appears between Ru foil and $RuCl_3$, but shifts toward $RuCl_3$, suggesting that the oxidation state of Ru species in Ru-$MLDZ_{2:1}$/AC is also between 0 and +3, but slightly higher than Ru/AC. After thermal reduction, the white line peak of Ru-$MLDZ_{2:1}$/AC-H_2 shifts to that of Ru foil, indicating an increased proportion of low-valent Ru species, which is consistent with the XPS results.

From the extended X-ray absorption fine structure (EXAFS) spectra of the reference samples of Ru foil, $RuCl_3$ and RuO_2, it can be observed that the characteristic peaks of the Ru–Ru, Ru–Cl, and Ru–O bonds appear at 2.67, 2.34, and 1.96 Å, respectively (Figs. 3(e)–3(g) and Table S6 in the ESM) [43]. In the benchmark Ru/AC catalyst, the Ru–Ru bond is also present in addition to Ru–Cl and Ru–C/N/O bonds, indicating the existence of nano-sized ruthenium species in the catalyst, which is consistent with the AC-HAADF-STEM characterization results. After ligand coordination, the Ru–C/N/O coordination number increases and the Ru–Ru coordination number decreases in the Ru-$MLDZ_{2:1}$/AC catalyst, indicating that the introduction of the ligand generates a strong interaction between the ligand and Ru precursor, which further disperses the Ru active species. This is consistent with the coexistence of single atoms and clusters in the AC-HAADF-STEM characterization results. After thermal reduction treatment of the Ru-$MLDZ_{2:1}$/AC catalyst (Ru-$MLDZ_{2:1}$/AC-H_2), the coordination number of Ru–C/N/O in the catalyst decreases, and no Ru–Ru species appear, indicating that the Ru species exist in a single-atom dispersed state, which is also confirmed by the results of AC-HAADF-STEM. The wavelet transform (WT) contour plot of the Ru K-edge EXAFS (Figs. 3(h) and 3(i) and Fig. S8 in the ESM) visually demonstrates the different coordination forms of Ru species in Ru-$MLDZ_{2:1}$/AC and Ru-$MLDZ_{2:1}$/AC-H_2 [44, 45]. The WT contour plot of Ru-$MLDZ_{2:1}$/AC exhibits a prominent feature at 1.5 Å, which is associated with Ru–C/N/O coordination, and another feature at 2.5 Å corresponds to Ru–Ru coordination, confirming the coexistence of single Ru atoms and small clusters. In contrast, the WT plot of Ru-$MLDZ_{2:1}$/AC-H_2 shows only the 1.5 Å

feature, corresponding exclusively to Ru–C/N/O coordination, confirming the presence of atomically dispersed Ru species. These results demonstrate that both the coordination interaction with imidazole ligands and the thermal reduction treatment synergistically promote the formation of Ru single-atom species.

3.3 Mechanism study of hydrosilylation of 1-hexene

To elucidate the reaction mechanism underlying the performance differences between Ru-MLDZ$_{2:1}$/AC-H$_2$ and Ru/AC, DFT calculations were conducted. Given the favorable coordination interaction between Ru and imidazole ligands, combined with insights from AC-HAADF-STEM imaging and EXAFS coordination analysis of Ru atoms, we rationally designed and constructed isolated Ru–N$_4$ sites (one Ru atom coordinated with four imidazole molecules) and Ru$_6$ nanoparticles on the graphene surface, representing Ru-MLDZ$_{2:1}$/AC-H$_2$ and Ru/AC catalysts, respectively (Fig. S9 in the ESM).

As illustrated in Fig. 4(a), both Ru-MLDZ$_{2:1}$/AC-H$_2$ and Ru/AC catalysts exhibit weak adsorption towards 1-hexene, whereas they demonstrate significantly stronger adsorption affinity for triethoxysilane. Notably, Ru-MLDZ$_{2:1}$/AC-H$_2$ displays a markedly higher adsorption energy for triethoxysilane (−2.215 eV) compared to Ru/AC (−0.894 eV). This disparity indicates that the active sites on the Ru-MLDZ$_{2:1}$/AC-H$_2$ catalyst surface are preferentially occupied by triethoxysilane molecules, which facilitates the activation of Si–H bond and thereby promotes the initiation of the hydrosilylation reaction [28].

Current research generally holds that the alkene hydrosilylation predominantly proceeds via two pathways [46–49] (Fig. 4(b)): the classical Chalk–Harrod mechanism and the modified Chalk–Harrod mechanism. According to the classical Chalk–Harrod mechanism, Ru-catalyzed alkene hydrosilylation proceeds in three steps: (Step i) The silane HSi(OC$_2$H$_5$)$_3$ chemisorbs at the Ru active site, where the Si–H bond undergoes oxidative addition and coordinates to the Ru center; (Step ii) the alkene inserts into the Ru–H bond to form an alkyl intermediate; (Step iii) reductive elimination forms the Si–C bond, releasing the target organosilane product. In the modified Chalk–Harrod mechanism, Step ii instead involves alkene insertion into the Ru–Si bond, followed by the reductive elimination to form the C–H bond.

The optimized configurations of the Step ii in the modified Chalk–Harrod mechanism for Ru-MLDZ$_{2:1}$/AC-H$_2$ and Ru/AC catalysts are identical to those in the classical Chalk–Harrod mechanism (Fig. S10 in the ESM). This observation can be attributed to the steric hindrance effect that prevents the insertion of 1-hexene molecule into the Ru–Si bond, suggesting that the classical Chalk–Harrod mechanism is more conducive to the progress of the reaction [50]. Figure 4(c) and Figs. S11 and S12 in the ESM depict the detailed energy profile along the classical Chalk–Harrod reaction pathway for both catalysts. According to the proposed catalytic cycle, the adsorption and activation step of silane (Step i) determines the duration of the induction period. The barrier (Step i) for Ru-MLDZ$_{2:1}$/AC-H$_2$ (0.077 eV) is substantially lower than that for Ru/AC (0.389 eV), thereby facilitating reaction initiation. In the subsequent alkene insertion step (Step ii), the reaction process of the two catalysts is exothermic. Significantly, the intermediate formed on Ru-MLDZ$_{2:1}$/AC-H$_2$ exhibits enhanced thermodynamic stability (−0.333 eV) relative to that on Ru/AC (−0.261 eV). In both the Ru-MLDZ$_{2:1}$/AC-H$_2$ and Ru/AC systems, the reductive elimination of Si–C (Step iii) exhibits the highest activation barrier, thereby constituting the rate-determining step (RDS). Notably, the activation barrier of RDS for Ru-MLDZ$_{2:1}$/AC-H$_2$ (0.132 eV) is significantly lower than that for Ru/AC (0.956 eV), indicating that the former system facilitates product desorption

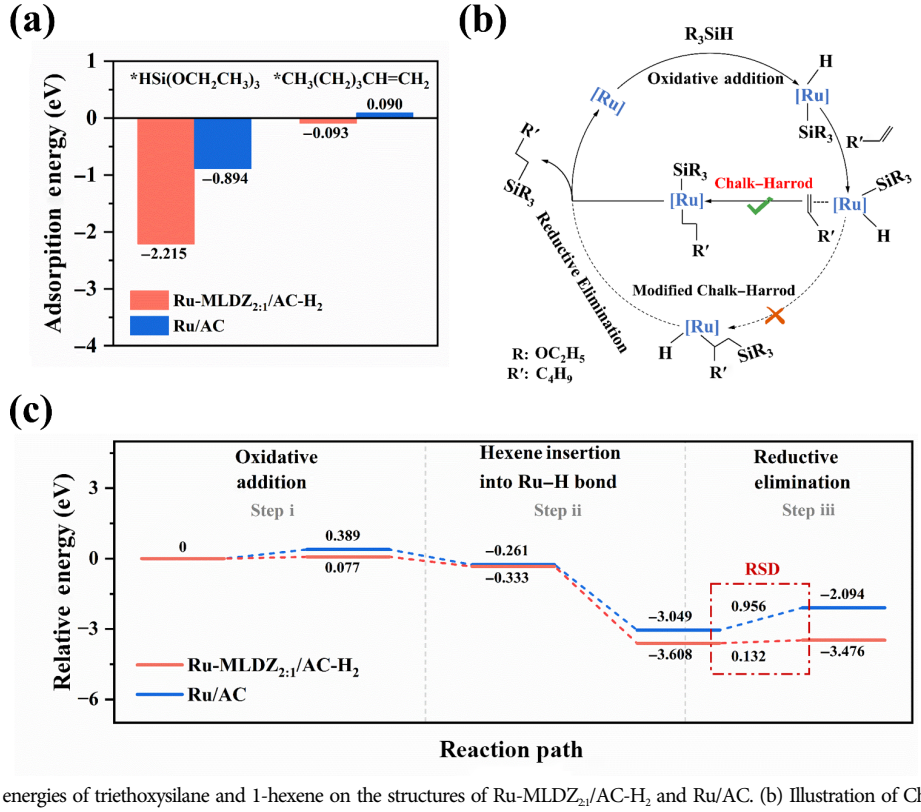

Figure 4 (a) Adsorption energies of triethoxysilane and 1-hexene on the structures of Ru-MLDZ$_{2:1}$/AC-H$_2$ and Ru/AC. (b) Illustration of Chalk–Harrod and modified Chalk–Harrod mechanism. (c) Classical Chalk–Harrod reaction pathway (energy profile) calculated for Ru-MLDZ$_{2:1}$/AC-H$_2$ and Ru/AC.

more effectively. These theoretical calculation results are in excellent agreement with the experimental results mentioned earlier, further revealing the reasons why the Ru-MLDZ$_{2:1}$/AC-H$_2$ manifests superior catalytic performance compared to the Ru/AC catalyst.

4 Conclusions

In summary, we have successfully developed a highly dispersed Ru single-atom catalyst (Ru-MLDZ$_{2:1}$/AC-H$_2$) via a ligand engineering-thermal reduction synergistic (LETRS) strategy. The resulting Ru-MLDZ$_{2:1}$/AC-H$_2$ catalyst demonstrates exceptional performance in the hydrosilylation of 1-hexene with TES. Multiscale characterization combined with theoretical calculations demonstrates that the unique Ru–N$_4$ coordination environment in Ru-MLDZ$_{2:1}$/AC-H$_2$ exhibits stronger adsorption toward triethoxysilane compared to Ru/AC, which facilitates Si–H bond activation and reduces the energy barrier of the rate-determining step, thereby exhibiting superior catalytic activity. This work establishes a solid experimental foundation for employing Ru-based catalysts in hydrosilylation reactions and provides a generalizable strategy for the rational design and construction of single-atom heterogeneous catalysts, offering important implications for developing next-generation industrial catalysts with enhanced efficiency and economic viability.

Electronic Supplementary Material: Supplementary material (including the details of characterization and computational methods, ICP results, XRD results, AC-HAADF-STEM images, BET data, XPS spectra and corresponding analysis results, EXAFS spectra, and DFT calculation results for different catalysts) is available in the online version of this article at https://doi.org/10.26599/NR.2026.94908513.

Data availability

All data needed to support the conclusions in the paper are presented in the manuscript and the Electronic Supplementary Material. Additional data related to this paper may be requested from the corresponding author upon request.

Acknowledgements

This work was supported by Bingtuan Talent - Youth Cultivation Program Project, the Tianchi Talent Project, Scientific and Technological Project of Yunnan Precious Metals Laboratory (No. YP2023050202), and the Project of Achievement Transformation and Technology Extension of Shihezi University (No. CGZH202302).

Declaration of competing interest

All the contributing authors report no conflict of interests in this work.

Author contribution statement

Y. L.: Data curation, writing – original draft, writing manuscript, experimental design. X. P. Y.: Formal analysis, visualization, resources. S. W.: Software, formal analysis. Y. Z. D.: Conceptualization, funding acquisition, resources, supervision, writing – review & editing. B. W.: Methodology, supervision. J. L. Z.: Conceptualization, supervision. H. Y. Z.: Conceptualization, supervision, validation, investigation, funding acquisition. All the authors have approved the final manuscript.

Use of AI statement

None.

References

[1] Liu, L.; Li, X. N.; Dong, H.; Wu, C. Hydrosilylation reaction of ethylene with triethoxysilane catalyzed by ruthenium halides and promoted by cuprous halides. *J. Organomet. Chem.* **2013**, *745–746*, 454–459.

[2] Nakajima, Y.; Shimada, S. Hydrosilylation reaction of olefins: Recent advances and perspectives. *RSC Adv.* **2015**, *5*, 20603–20616.

[3] Galeandro-Diamant, T.; Sayah, R.; Zanota, M. L.; Marrot, S.; Veyre, L.; Thieuleux, C.; Meille, V. Pt nanoparticles immobilized in mesostructured silica: A non-leaching catalyst for 1-octene hydrosilylation. *Chem. Commun.* **2017**, *53*, 2962–2965.

[4] Hu, M. Y.; He, Q.; Fan, S. J.; Wang, Z. C.; Liu, L. Y.; Mu, Y. J.; Peng, Q.; Zhu, S. F. Ligands with 1,10-phenanthroline scaffold for highly regioselective iron-catalyzed alkene hydrosilylation. *Nat. Commun.* **2018**, *9*, 221.

[5] Chen, Y. J.; Ji, S. F.; Sun, W. M.; Chen, W. X.; Dong, J. C.; Wen, J. F.; Zhang, J.; Li, Z.; Zheng, L. R.; Chen, C. et al. Discovering partially charged single-atom Pt for enhanced anti-Markovnikov alkene hydrosilylation. *J. Am. Chem. Soc.* **2018**, *140*, 7407–7410.

[6] Marciniec, B. Catalysis by transition metal complexes of alkene silylation-recent progress and mechanistic implications. *Coord. Chem. Rev.* **2005**, *249*, 2374–2390.

[7] Obligacion, J. V.; Chirik, P. J. Earth-abundant transition metal catalysts for alkene hydrosilylation and hydroboration. *Nat. Rev. Chem.* **2018**, *2*, 15–34.

[8] de Almeida, L. D.; Wang, H. L.; Junge, K.; Cui, X. J.; Beller, M. Recent advances in catalytic hydrosilylations: Developments beyond traditional platinum catalysts. *Angew. Chem., Int. Ed.* **2021**, *60*, 550–565.

[9] Tondreau, A. M.; Atienza, C. C. H.; Weller, K. J.; Nye, S. A.; Lewis, K. M.; Delis, J. G. P.; Chirik, P. J. Iron catalysts for selective anti-Markovnikov alkene hydrosilylation using tertiary silanes. *Science* **2012**, *335*, 567–570.

[10] Du, X. Y.; Zhang, Y. L.; Peng, D. J.; Huang, Z. Base-metal-catalyzed regiodivergent alkene hydrosilylations. *Angew. Chem., Int. Ed.* **2016**, *55*, 6671–6675.

[11] Speier, J. L.; Webster, J. A.; Barnes, G. H. The addition of silicon hydrides to olefinic double bonds. Part II. The use of group VIII metal catalysts. *J. Am. Chem. Soc.* **1957**, *79*, 974–979.

[12] Karstedt, B. D. Platinum complexes of unsaturated siloxanes and platinum containing organopolysiloxanes. U.S. Patent 3775452-A, November 27, 1973.

[13] Li, X. N.; Yang, X. F.; Huang, Y. Q.; Zhang, T.; Liu, B. Supported noble-metal single atoms for heterogeneous catalysis. *Adv. Mater.* **2019**, *31*, 1902031.

[14] Yang, H.; Zhou, Z. J.; Tang, C. H.; Chen, F. Recent advances in heterogeneous hydrosilylation of unsaturated carbon–carbon bonds. *Chin. Chem. Lett.* **2024**, *35*, 109257.

[15] Lee, E. K.; Park, S. A.; Woo, H.; Park, K. H.; Kang, D. W.; Lim, H.; Kim, Y. T. Platinum single atoms dispersed on carbon nanotubes as reusable catalyst for Suzuki coupling reaction. *J. Catal.* **2017**, *352*, 388–393.

[16] Planellas, M.; Guo, W. S.; Alonso, F.; Yus, M.; Shafir, A.; Pleixats, R.; Parella, T. Hydrosilylation of internal alkynes catalyzed by tris-imidazolium salt-stabilized palladium nanoparticles. *Adv. Synth. Catal.* **2014**, *356*, 179–188.

[17] Hu, S. P.; Lei, H. F.; Shi, J. L.; Ye, Y. J.; Peng, F. L.; Wu, W. L.; Zhang, J.; Yan, H.; Ma, C.; Zeng, J. CeO_2-supported bi-layer Pt clusters for anti-Markovnikov alkene hydrosilylation. *Sci. China Chem.* **2026**, *69*, 9946–952.

[18] Lu, M. G.; Kang, X. X.; Qian, C. J.; Wang, K. Y.; Ren, X. Y.; Wang, R. H.; Sun, K.; Chen, Z.; Duan, X. M.; Tian, S. B. Modeled single-atomic-site Pt catalyst with well-defined coordination structure for hydrosilylation reaction. *Angew. Chem., Int. Ed.* **2025**, *64*, e202508064.
[19] Tanaka M.; Hayashi T.; Mi Z. Y. Ruthenium complex-catalyzed hydrosilylation of allyl chloride with trimethoxysilane. *J. Mol. Catal.* **1993**, *81*, 207–214.
[20] Kanbur, U.; Witzke, R. J.; Xu, J. Y.; Ferrandon, M. S.; Goetjen, T. A.; Kropf, A. J.; Perras, F. A.; Liu, C.; Tilley, T. D.; Kaphan, D. M. et al. Supported electrophilic organoruthenium catalyst for the hydrosilylation of olefins. *ACS Catal.* **2023**, *13*, 13383–13394.
[21] Zhu, Y. Q.; Cao, T.; Cao, C. B.; Luo, J.; Chen, W. X.; Zheng, L. R.; Dong, J. C.; Zhang, J.; Han, Y. H.; Li, Z. et al. One-pot pyrolysis to N-doped graphene with high-density Pt single atomic sites as heterogeneous catalyst for alkene hydrosilylation. *ACS Catal.* **2018**, *8*, 10004–10011.
[22] Ji, S. F.; Chen, Y. J.; Wang, X. L.; Zhang, Z. D.; Wang, D. S.; Li, Y. D. Chemical synthesis of single atomic site catalysts. *Chem. Rev.* **2020**, *120*, 11900–11955.
[23] Duan, X. X.; Niu, B.; Wang, Y. W.; Yang, Z. W.; Ren, H. N.; Li, G. G.; Wei, Z.; Cheng, J.; Zhang, Z. S.; Hao, Z. P. Regulating the electronic metal–support interaction of single-atom ruthenium catalysts for boosting chlorobenzene oxidation. *Environ. Sci. Technol.* **2025**, *59*, 7408–7418.
[24] Ye, B. C.; Li, W. H.; Zhang, X.; Chen, J.; Gao, Y.; Wang, D. S.; Pan, H. G. Advancing heterogeneous organic synthesis with coordination chemistry-empowered single-atom catalysts. *Adv Mater.* **2024**, *36*, 2402747.
[25] Wei, Y. S.; Zhang, M.; Zou, R. Q.; Xu, Q. Metal–organic framework-based catalysts with single metal sites. *Chem. Rev.* **2020**, *120*, 12089–12174.
[26] Pei, S. K.; Wang, S.; Lu, Y. X.; Li, X.; Wang, B. Application of metal-based catalysts for Fenton reaction: From homogeneous to heterogeneous, from nanocrystals to single atom. *Nano Res.* **2024**, *17*, 9446–9471.
[27] Han, Y. H.; Xiong, Y.; Liu, C. W.; Zhang, H. W.; Zhao, M. Q.; Chen, W.; Chen, W. X.; Huang, W. Electron-rich isolated Pt active sites in ultrafine $PtFe_3$ intermetallic catalyst for efficient alkene hydrosilylation. *J. Catal.* **2021**, *396*, 351–359.
[28] Yang, C. L.; Tong, J. M.; Li, H. L.; Gao, H. Y.; Wen, G. D.; Zhang, J. S.; Yan, Y. K. Interfacial spontaneous reduction strategy to synthesize low-valent Pt single-atom catalyst for boosting hydrosilylation. *ACS Catal.* **2024**, *14*, 2341–2349.
[29] Li, M. Y.; Zhao, S.; Li, J.; Chen, X.; Ji, Y. J.; Yu, H. J.; Bai, D. R.; Xu, G. W.; Zhong, Z. Y.; Su, F. B. Partially charged single-atom Ru supported on ZrO_2 nanocrystals for highly efficient ethylene hydrosilylation with triethoxysilane. *Nano Res.* **2022**, *15*, 5857–5864.
[30] Lu, Y. B.; Lin, F.; Zhang, Z. H.; Thompson, C.; Zhu, Y. F.; Doudin, N.; Kovarik, L.; Vargas, C. E. G.; Jiang, D.; Fulton, J. L. et al. Enhancing activity and stability of Pd-on-TiO_2 single-atom catalyst for low-temperature CO oxidation through *in-situ* local environment tailoring. *J. Am. Chem. Soc.* **2024**, *146*, 28141–28152.
[31] Yin, S. H.; Li, Y. R.; Yang, J.; Liu, J.; Yang, S. L.; Cheng, X. Y.; Huang, H.; Huang, R.; Wang, C. T.; Jiang, Y. X. et al. Unveiling low temperature assembly of dense Fe–N_4 active sites via hydrogenation in advanced oxygen reduction catalysts. *Angew. Chem., Int. Ed.* **2024**, *63*, e202404766.
[32] Tao, H. C.; Choi, C.; Ding, L. X.; Jiang, Z.; Han, Z. S.; Jia, M. W.; Fan, Q.; Gao, Y. N.; Wang, H. H.; Robertson, A. W. et al. Nitrogen fixation by Ru single-atom electrocatalytic reduction. *Chem* **2019**, *5*, 204–214.
[33] Wu, T.; Hong, J.; Lu, Z. W.; Wu, H. Y.; Wu, C. Z.; Tang, Z. B.; Liu, X. H.; Zeng, B. R.; Xu, Y. T.; Chen, G. R. et al. *In-situ* generation of Ru-catechol coordinative polymer precursor for high-performance hydrogen evolution reaction doped carbon catalyst. *Appl. Catal. B: Environ.* **2021**, *285*, 119795.
[34] Guo, H. R.; Wang, G. H.; Zhang, B.; Li, J. K.; Sui, W. J.; Jia, H. Y.; Si, C. L. Ultrafine Ru nanoparticles deposited on lignin-derived nitrogen-doped carbon nanolayer for the efficient conversion of levulinic acid to γ-valerolactone. *Renew. Energy* **2024**, *222*, 119954.
[35] Li, B. Y.; Zhao, H. C.; Fang, J.; Li, J. F.; Gao, W.; Ma, K. X.; Liu, C.; Yang, H. R. Y.; Ren, X. G.; Dong, Z. P. Ru nanoparticles anchored on porous N-doped carbon nanospheres for efficient catalytic hydrogenation of levulinic acid to γ-valerolactone under solvent-free conditions. *J. Colloid Interface Sci.* **2022**, *623*, 905–914.
[36] Liu, P. F.; Zheng, C. L.; Liu, W.; Wu, X. D.; Liu, S. Oxidative redispersion-derived single-site Ru/CeO_2 catalysts with mobile Ru complexes trapped by surface hydroxyls instead of oxygen vacancies. *ACS Catal.* **2024**, *14*, 6028–6044.
[37] Xiong, M.; Gao, Z.; Qin, Y. Spillover in heterogeneous catalysis: New insights and opportunities. *ACS Catal.* **2021**, *11*, 3159–3172.
[38] Yan, Z. Y.; Wang, X. F.; Zhang, Y. F.; Zhang, Z. Y.; Qi, L.; Miao, B. R.; Li, Q. B. Insights into reverse oxygen spillover effect induced via CeO_2 modulation to enhance the stability of $CuCoO_x$ catalysts in hydrodeoxygenation of biomass derivatives. *Appl. Catal. B: Environ. Energy* **2024**, *358*, 124389.
[39] Wang, J.; Fang, W. H.; Hu, Y.; Zhang, Y. H.; Dang, J. Q.; Wu, Y.; Chen, B. Z.; Zhao, H.; Li, Z. X. Single atom Ru doping 2H-MoS_2 as highly efficient hydrogen evolution reaction electrocatalyst in a wide pH range. *Appl. Catal. B: Environ.* **2021**, *298*, 120490.
[40] Ding, Y.; Li, X. H.; Pan, H. Y.; Wu, P. Ru nanoparticles entrapped in ordered mesoporous carbons: An efficient and reusable catalyst for liquid-phase hydrogenation. *Catal. Lett.* **2014**, *144*, 268–277.
[41] Ravel, B.; Newville, M. *ATHENA, ARTEMIS, HEPHAESTUS*: Data analysis for X-ray absorption spectroscopy using *IFEFFIT*. *J. Synchrotron Radiat.* **2005**, *12*, 537–541.
[42] Zabinsky, S. I.; Rehr, J. J.; Ankudinov, A.; Albers, R. C.; Eller, M. J. Multiple-scattering calculations of X-ray-absorption spectra. *Phys. Rev. B* **1995**, *52*, 2995–3009.
[43] Zhou, Y. L.; Wei, F. F.; Qi, H. F.; Chai, Y. C.; Cao, L. R.; Lin, J.; Wan, Q.; Liu, X. Y.; Xing, Y.; Lin, S. et al. Peripheral-nitrogen effects on the Ru_1 centre for highly efficient propane dehydrogenation. *Nat. Catal.* **2022**, *5*, 1145–1156.
[44] Funke, H.; Scheinost, A. C.; Chukalina, M. Wavelet analysis of extended X-ray absorption fine structure data. *Phys. Rev. B* **2005**, *71*, 094110.
[45] Wang, S. Z.; Zhang, K. L.; Li, H. L.; Xiao, L. P.; Song, G. Y. Selective hydrogenolysis of catechyl lignin into propenylcatechol over an atomically dispersed ruthenium catalyst. *Nat. Commun.* **2021**, *12*, 416.
[46] Thankachan, A. P.; Afsina, C. M. A.; Shamna, S.; Anilkumar, G. Recent advances in ruthenium-catalyzed hydrosilylation of unsaturated compounds: Applications and mechanistic studies. *Results Chem.* **2022**, *4*, 100511.
[47] Glaser, P. B.; Tilley, T. D. Catalytic hydrosilylation of alkenes by a ruthenium silylene complex. Evidence for a new hydrosilylation mechanism. *J. Am. Chem. Soc.* **2003**, *125*, 13640–13641.
[48] Beddie, C.; Hall, M. B. A theoretical investigation of ruthenium-catalyzed alkene hydrosilation: Evidence to support an exciting new mechanistic proposal. *J. Am. Chem. Soc.* **2004**, *126*, 13564–13565.
[49] Smith, P. W.; Dong, Y. Y.; Tilley, T. D. Efficient and selective alkene hydrosilation promoted by weak, double Si–H activation at an iron center. *Chem. Sci.* **2020**, *11*, 7070–7075.
[50] Li, R. L.; Yu, G.; Lin, Z.; Lin, X.; Du, J. Y.; Gao, X. P.; Su, C. L.; Wu, Y. Stabilizing few-atom platinum clusters by zinc single-atom-glue for efficient anti-Markovnikov alkene hydrosilylation. *Angew. Chem., Int. Ed.* **2024**, *63*, e202404568.